Electrohydrodynamic flow around a colloidal particle near an electrode with an oscillating potential

W. D. RISTENPART, I. A. AKSAY AND D. A. SAVILLE

Department of Chemical Engineering, Princeton University, Princeton, NJ 08544, USA

Electrohydrodynamic (EHD) flow around a charged spherical colloid near an electrode was studied theoretically and experimentally to understand the nature of long-range particle–particle attraction near electrodes. Numerical computations for finite double-layer thicknesses confirmed the validity of an asymptotic methodology for thin layers. Then the electric potential around the particle was computed analytically in the limit of zero Péclet number and thin double layers for oscillatory electric fields at frequencies where Faradaic reactions are negligible. Streamfunctions for the steady component of the EHD flow were determined with an electro-osmotic slip boundary condition on the electrode surface. Accordingly, it was established how the axisymmetric flow along the electrode is related to the dipole coefficient of the colloidal particle. Under certain conditions, the flow is directed toward the particle and decays as r^{-4}, in accord with observations of long-range particle aggregation. To test the theory, particle-tracking experiments were performed with fluorescent 300 nm particles around 50 μm particles over a wide range of electric field strengths and frequencies. Treating the particle surface conductivity as a fitting parameter yields velocities in excellent agreement with the theoretical predictions. The observed frequency dependence, however, differs from the model predictions, suggesting that the effect of convection on the charge distribution is not negligible as assumed in the zero Péclet number limit.

1. Introduction

Every electrokinetic process involves field-induced motion. In capillary electrophoresis, particle motion is a combination of translation, owing to the particle charge, and electro-osmotic flow, arising from charge on the capillary wall (Russel, Saville & Schowalter 1991). Electric fields are also involved in the separation of DNA and other macromolecules (Dai *et al.* 2003; Tegenfeldt *et al.* 2004) and in positioning particles or biological cells (Stone, Stroock & Ajdari 2004; Bhatt, Gregio & Velev 2005). Charged particles immobilized in microfluidic networks can be used for pumping or mixing (Squires & Bazant 2004). Recent work in microfluidics has focused attention on the manipulation of fluids and particles at small length scales (Stone & Kim 2001; Whitesides & Stroock 2001; Bazant & Squires 2004). A major outstanding issue concerns the details of the flow around particles near an electrode inasmuch as such flows are involved in electrohydrodynamic (EHD) particle assembly processes. The current work establishes a theoretical model for these flows.

Although isolated particles have received considerable attention, there has been little study of particle behaviour near electrodes, despite its many applications and fascinating character. For example, particles widely dispersed across an electrode

form planar crystalline aggregates in steady or oscillatory fields (Böhmer 1996; Trau, Saville & Aksay 1996). Moreover, since the particles are electrostatically repulsive, aggregation is unexpected given the presence of Coulombic and induced-dipole repulsion. Nevertheless, particles migrate over extended distances (five to ten particle radii) to create large planar structures that disintegrate when the field is removed. The assembly of particles with electric fields is an example of 'guided self-assembly,' a subject of considerable technological promise (Whitesides & Grzybowski 2002). Electric fields may be useful in guiding the self-assembly of photonic band-gap materials (Joannopoulos 2001); biosensors (Velev & Kaler 1999) and lab-on-a-chip (Gau *et al.* 1999) devices also benefit from electric-field patterning of colloids coated with specific biological or catalytic molecules.

In their investigation of the field-induced layering of colloidal crystals, Trau *et al.* (1996, 1997) put forward an EHD mechanism wherein distortions of the electric field alter the body-force distribution in the electrode's charge polarization layer. The action of the applied field on this charge produces flow and, since the induced charge and the electrical body force are each proportional to the applied voltage, the flow scales on the square of the field strength. In an oscillatory field, the flow has a steady component wherein nearby particles are mutually entrained and carried toward one another. We studied EHD aggregation of this sort experimentally (Ristenpart *et al.* 2004) by modelling the particle's effect as a perturbation of the electric field due to a 'point-dipole'. We found that aggregation rates scale on the (complex) dipole coefficient and therefore decay inversely with frequency. According to our analysis, motion is directed towards a test particle in typical circumstances, which is consistent with the observed aggregation phenomena.

Thus, although it is now acknowledged that fluid motion plays a central role in particle aggregation in electric fields (Trau *et al.* 1996; Sides 2001; Ristenpart *et al.* 2004), there is less agreement as to the details of the flow. Most authors simply refer to the electric-field-induced flow as a source of 'attraction' (Gong & Marr 2001; Gong, Wu & Marr 2002; Nadal *et al.* 2002). Some even explain aggregation in thermodynamic terms (Zhang & Liu 2004).

The lack of consensus is partly because most studies focus on aggregation (Solomentsev *et al.* 2000; Nadal *et al.* 2002; Ristenpart *et al.* 2004). Only two reports recount observations of flow, and neither presents a comprehensive picture. Yeh, Seul & Shraiman (1997) recount seeing tracers move in a 'toroidal' fashion near a particle in an unspecified electric field; Nadal *et al.* (2002) noted tracer particle motion in a 'centripetal' flow field around a larger particle. The paucity of experimental studies is matched by a dearth of theoretical work.

The goal of the current work is to elucidate the nature of electric-field-induced flow around a particle near an electrode with an oscillating potential; in the aggregation process, particles are carried towards one another by the superposition of such flows. The presentation is divided into two parts: a theoretical study and an experimental corroboration of the theory.

The theoretical analysis is, necessarily, incomplete. The governing equations for the standard electrokinetic model for flow around a particle near an electrode with the customary boundary conditions (i.e. specified potential and current on the electrodes) are, in principle, readily soluble using standard numerical techniques. Unfortunately, difficulties with a purely numerical approach arise from disparities between the Debye length, κ^{-1}, the particle radius, a, and the particle–electrode separation, h. Because $\kappa a \gg 1$, the numerical problem is 'stiff' and computational limitations thwart resolution.

Analytical approaches are also difficult, and even a linearized version of the standard electrokinetic model yields a complicated set of coupled partial differential equations with no known analytical solution. When $\kappa a \gg 1$, however, it is appropriate to analyse the limiting case where free charge is negligible throughout most of the domain of interest and this offers an opportunity to use asymptotic methods. Accordingly, the electric field can be described by solutions to Laplace's equation and transport processes near the particle surface represented with an adaptation of Bikerman's model for surface transport to provide boundary conditions (Bikerman 1939; O'Brien 1986).

Another complication arises when specifying boundary conditions on the electrode in the limit of thin double layers. Specification of a constant potential along the electrode, as used in previous analyses of electrophoretic processes near electrodes (Morrison & Stukel 1970; Reed & Morrison 1976), omits the presence of tangential potential gradients in the outer part of the polarization layer that give rise to EHD flow. Perturbation methods using current conservation boundary conditions (Gonzalez *et al.* 2000; Squires & Bazant 2004) require more than the lowest-order terms to capture lateral variations in charge and field in and near the diffuse region.

Numerical work (§3) demonstrates, however, that the situation near the electrode is simplified in the appropriate limits. Even in the presence of a particle, the electric field strength near the electrode underneath a particle approaches a laterally uniform state (i.e. $\boldsymbol{E} \cdot \boldsymbol{n} \approx$ constant) as the Debye length decreases, provided the particle is not too close to the electrode. Use of a constant-field-strength boundary condition provides a route to analytical solutions for both the electric field and the EHD flow. These describe the structure of the flow around a single particle for large values of κa where numerical solutions are infeasible, making comparison with the experimental results straightforward.

The experimental work involves particle-tracking velocimetry which, despite complications due to particle size, yields extensive quantitative information. In electrically driven assemblies, one is concerned with flows near, say, 100 nm particles, but the details of such flows are too small to be imaged by optical microscopy. Accordingly, EHD flow was traced near a large ($\sim$50 μm) sphere using small ($\sim$300 nm) fluorescent particles. The agreement between theory and experiment shows that the EHD model is appropriate and can be applied in order to understand processes with smaller particles, when viewed in the proper dimensionless context.

The paper is organized as follows. First, in §2, the potential between parallel electrodes is studied in the framework of the standard electrokinetic model. The model indicates that the field strength outside the polarization layers approaches a constant value at the appropriate frequencies. In §3, the effects of a particle near an electrode are explored numerically for modest size values of κa using a finite-element scheme. Although the particle distorts the electric field strength near the electrode beneath the particle, the calculations indicate that as $\kappa^{-1} \to 0$ (i.e. as the thickness of the polarization layer becomes infinitesimal), the field strength in the gap at the edge of the polarization layer becomes progressively more uniform. A constant field strength condition makes analytical solutions feasible.

An analytical solution for the electric potential with the constant-field-strength boundary condition is presented in §4. With the thin-double-layer approximation, Laplace's equation governs the potential and it can be solved by separation of variables in bispherical coordinates. This shows that surface transport along the particle surface (which determines the particle dipole coefficient) has a pronounced effect on the electric potential and the consequent fluid flow.

The solution for the electric potential is used in §5 to work out the axisymmetric streamfunction for flow around a particle near an electrode. Under typical conditions, an EHD flow is directed inward toward a 'test' particle and decays as r^{-4}.

Experimental information about the EHD flow around a particle near an electrode is presented in §6. Submicrometre fluorescent tracer particles were tracked around a single (large) particle over a range of applied potentials and frequencies. Measurements of the tracer velocities agree with the analytical theory when the particle surface conductivity is used as a fitting parameter. The paper concludes in §7 with a summary of the theoretical and experimental results.

2. The electric potential between parallel electrodes

2.1. *The electrokinetic model*

The theory is based on the standard electrokinetic model as set out by Russel *et al.* (1991). Thus, fluid motion is described by the Stokes equations for low-Reynolds-number flows with an additional body force due to the presence of free charge. Ion motion is a combination of diffusion, electromigration and convection while electrostatic potential and charge are related by the Gauss equation. Here we focus on 1-1 electrolytes with ions of equal mobilities (in water at 298 K, the diffusivities of potassium and chloride ions differ by less than 5 %) and the field equations are:

$$0 = -\nabla P - e(n^+ - n^-)\boldsymbol{E} + \mu\nabla^2\boldsymbol{u}, \tag{2.1}$$

$$\nabla \cdot \boldsymbol{u} = \boldsymbol{0}, \tag{2.2}$$

$$\frac{\partial n^\pm}{\partial t} = D\nabla^2 n^\pm \pm e\frac{D}{k_B T}\nabla \cdot (n^\pm \nabla\phi) - \boldsymbol{u} \cdot \nabla n^\pm, \tag{2.3}$$

$$\varepsilon\varepsilon_o \nabla^2 \phi = -e(n^+ - n^-). \tag{2.4}$$

The symbols have their usual meanings: P, pressure; e, charge on a proton; $n^\pm$, number densities of ions with positive or negative valences; $\boldsymbol{E}$, electric field strength; μ, viscosity; $\boldsymbol{u}$, velocity; D, ion diffusivity; $k_B T$, the product of Boltzmann's constant and the absolute temperature; ϕ, electric potential; ε, dielectric constant of the liquid; and ε_0, permittivity of free space. Equation (2.1) represents the usual momentum balance in the limit of negligible inertia, with an electric body force term. The number densities of ions are related to the electric field through Gauss's equation (2.4), and also by the conservation relation expressed in (2.3). Here, we have employed the Nernst–Planck equation to express the flux of ions; the three terms on the right-hand side of (2.3) represent diffusion, electromigration and convection, respectively.

This is essentially the model studied for isolated spheres and binary electrolytes by O'Brien & White (1978) and Delacey & White (1981). Their results were extended by Mangelsdorf & White (1992) to include inertial effects at higher frequencies. However, since those analyses rely on the symmetry of fields around an isolated sphere in a uniform field, they are not readily applicable to a particle near a boundary. Here, we use the model to investigate the situation between parallel electrodes and then for a sphere near an electrode.

2.2. *Oscillatory fields*

Consider two parallel electrodes, separated by a distance $2H$, with the centreline at $z = 0$ and an oscillatory potential $\Delta\phi e^{-i\omega t}$ applied on the electrode at $z = -H$ while the other is grounded. The velocity is zero everywhere and osmotic pressure balances

the electrostatic body force. Although the flux of ions at each electrode depends on the nature of the electrochemical reactions, the influence of Faradaic processes diminishes as the frequency of the applied potential increases. If the electrodes are 'perfectly polarizable', the flux of ions across the electrodes-electrolyte interface vanishes, i.e. at $z = \pm H$,

$$0 = -D \frac{dn^{\pm}}{dz} \mp \frac{eDn^{\pm}}{k_B T} \frac{d\phi}{dz}. \tag{2.5}$$

The assumption of perfect polarization specifically precludes consideration of flow phenomena associated with the production of ions via Faradaic reactions (Sides 2001; Fagan, Sides & Prieve 2002). Aggregation occurs at higher frequencies (~ 1 kHz) where Faradaic reactions are negligble, and the goal of this work is to identify the simplest model that elucidates EHD flow in the presence of a nearby particle.

For $\Delta\phi \ll k_B T/e$, Hollingsworth & Saville (2003) show that for a quiescent liquid, the linearized model leads to

$$\phi = \frac{\Delta\phi}{2} \left[1 - \frac{\sinh(\gamma z/H)\operatorname{csch}(\gamma) - i(z/H)\gamma \nu^2 \coth\gamma}{1 - i\gamma \nu^2 \coth\gamma} \right] e^{-i\omega t}. \tag{2.6}$$

Here, γ is

$$\gamma^2 = (\kappa H)^2 - i\frac{\omega H^2}{D}, \tag{2.7}$$

ν^2 is a dimensionless time scale,

$$\nu^2 = \frac{\omega}{\kappa^2 D}, \tag{2.8}$$

and the Debye length for a 1-1 electrolyte is

$$\kappa^{-1} = \sqrt{\frac{\varepsilon\varepsilon_0 k_B T}{2e^2 n_{\infty}}}; \tag{2.9}$$

n_{∞} is the ion density in the bulk. Although the potential depends on oscillation frequency in a complicated fashion, for frequencies in the range

$$\kappa D/H \ll \omega \ll \kappa^2 D, \tag{2.10}$$

the expression simplifies considerably. At the conditions of interest here, these frequencies are 10^2 and 10^7 Hz, and the field strength becomes

$$E \approx \frac{\Delta\phi}{2H} \left[\left(1 + \kappa H \left(\frac{\kappa D}{\omega H} \right)^2 \frac{\cosh(\kappa z)}{\sinh(\kappa H)} \right) - i \left(\frac{\kappa D}{\omega H} - \frac{\kappa^2 D}{\omega} \frac{\cosh(\kappa z)}{\sinh(\kappa H)} \right) \right] e^{-i\omega t}. \tag{2.11}$$

Outside polarization layers near the electrodes (with characteristic length κ^{-1}), the field strength is spatially uniform, i.e.

$$E \approx \frac{\Delta\phi}{2H} \left(1 - i\frac{\kappa D}{\omega H} \right) e^{-i\omega t}. \tag{2.12}$$

Since $\kappa D/\omega H \ll 1$, the field strength is largely in-phase with the applied potential. Inside the polarization layers, the electric field strength is much larger than $\Delta\phi/2H$ and, because of the motion of free charge, there is a large phase difference with the imposed potential. Figure 1 depicts the real component of the electric field strength and illustrates the transition from the polarization layer to the bulk. The charge
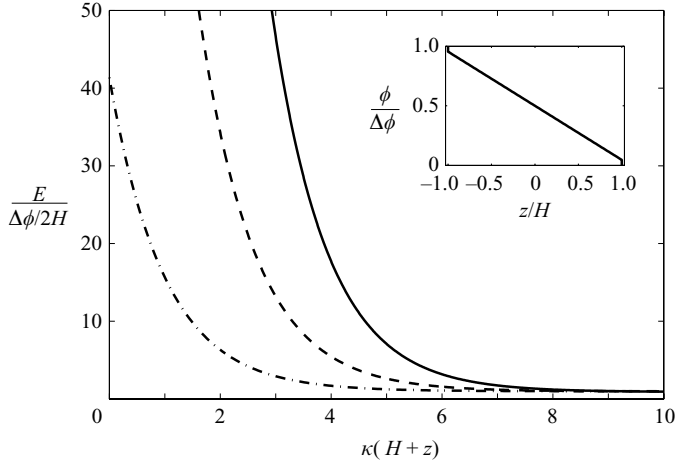
FIGURE 1. The real part of the dimensionless electric field strength, $E/(\Delta\phi/2H)$, between parallel electrodes with an oscillatory applied potential at different frequencies, at $\omega t = 2\pi$. $-\cdot-$, $\omega = 5\,\text{kHz}$; $---$, $\omega = 2\,\text{kHz}$; ——, $\omega = 1\,\text{kHz}$. Note that for $\kappa(H+z) \gg 1$, $E/(\Delta\phi/2H) \to 1$. Inset: the dimensionless potential $\phi/\Delta\phi$ across the cell for $\omega = 1\,\text{kHz}$. The potential varies linearly, except very close to $z/H = \pm 1$ (not discernible on the scale of this plot). $\kappa^{-1} = 10\,\text{nm}$, $H = 100\,\mu\text{m}$, $D = 2 \times 10^{-9}\,\text{m}^2\,\text{s}^{-1}$.

density at the edge of the polarization layer near the powered electrode is

$$q = \varepsilon\varepsilon_0 \left.\frac{\partial\phi}{\partial z}\right|_{z=-H} = \varepsilon\varepsilon_0 \frac{\Delta\phi}{2H}\left(1 + \mathrm{i}\frac{\kappa^2 D}{\omega}\right)\mathrm{e}^{-\mathrm{i}\omega t}, \tag{2.13}$$

for $\kappa D/H \ll \omega \ll \kappa^2 D$. As the expression indicates, the total charge density has an appreciable phase lag and decays inversely with frequency. This decay is a consequence of the finite mobility of ions; as the applied frequency increases, the ions have less time to move in response to the field, and the total charge consequently decreases.

3. The electric potential near an electrode in the presence of a particle: numerical solutions

3.1. *Background*

The potential distribution between parallel electrodes is straightforward because there are only two length scales: the Debye length and the electrode separation. The presence of a particle complicates matters by introducing two additional scales: the particle radius and the distance, h, between the electrode and particle surface. By restricting attention to situations where H is large, i.e. $H \gg a$ and $H \gg h$, the electrode separation may be ignored. Then the domain can be treated as semi-infinite, with a far-field condition equivalent to the uniform field in the absence of the particle. Here, numerical methods are used to explore the region near the electrode underneath a particle. The objective is to establish the extent to which the particle alters the structure of the electrode polarization layer. The numerical studies show that, providing the polarization layer is thin and the particle is well outside the layer, the particle 'sees' a uniform field strength along the electrode.
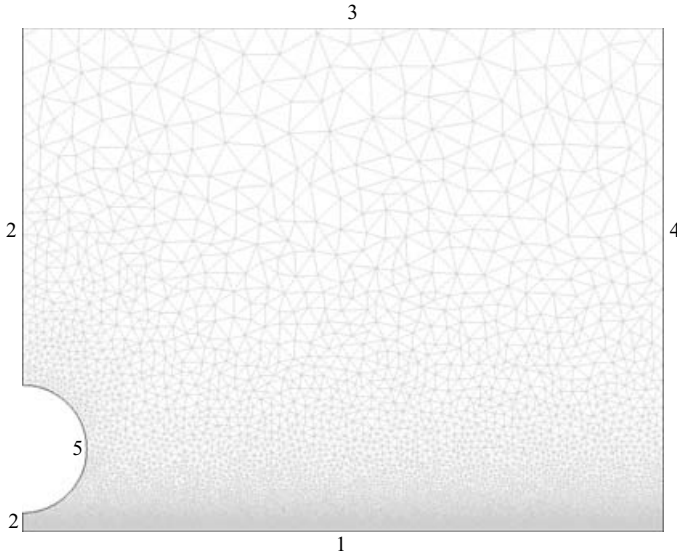
FIGURE 2. Representative domain and mesh for the finite-element analysis. The numbers identify regions where the boundary conditions are applied. To capture the steep potential and charge gradient, the mesh density increases close to boundary 1. Note that the figure is not to scale and the domain was truncated to fit boundary 3 into the diagram. The width of the domain was chosen such that the influence of the particle was negligible at boundary 4; typical domain widths ranged from 10 to 20 particle radii.

3.2. *Numerical model*

The linearized model, (2.1)–(2.4), was solved for a sphere near an electrode. For weak flows, the equations for the potential and free charge are decoupled from the fluid flow and the velocity field can be obtained after the potential and charge distributions are calculated. Omitting convective contributions to the free charge distribution is justified if the Péclet number based on a characteristic velocity, u_o, is small (Squires & Bazant 2004). According to our measurements (cf. §6), the flow speed underneath a 50 μm test particle is $\sim 25\ \mu\text{m s}^{-1}$ and this makes $au_o/D \leqslant 1$. In addition, convective effects sweep charge toward the particle so as to even out perturbations caused by the particle's proximity to the electrode. Accordingly, we assume that convective effects are unimportant.

It is useful to work with the equations in dimensionless form with the origin of a polar cylindrical coordinate system centred on the electrode below the spherical particle. Accordingly, the potentials are scaled on $k_B T/e$, lengths on the particle radius, and the dimensionless charge expressed as $\bar{n} \equiv (n^+ - n^-)/n_\infty$.

The boundary conditions are as follows (cf. figure 2). At the electrode (boundary 1) the potential is uniform and the ion flux vanishes,

$$\bar{\phi} = (e\Delta\phi/k_B T)\exp(-i\omega t), \quad 2\frac{\partial\bar{\phi}}{\partial\bar{z}} + \frac{\partial\bar{n}}{\partial\bar{z}} = 0, \quad \bar{z} = 0. \tag{3.1}$$

At the left-hand edge of the domain (boundary 2), radial derivatives vanish,

$$\frac{\partial\bar{\phi}}{\partial\bar{r}} = 0, \quad \frac{\partial\bar{n}}{\partial\bar{r}} = 0, \quad \bar{r} = 0. \tag{3.2}$$

At the outer edge of the domain (boundary 4), the potential and charge density asymptote to constant values so

$$\frac{\partial \bar{\phi}}{\partial \bar{r}} = 0, \quad \frac{\partial \bar{n}}{\partial \bar{r}} = 0, \quad \bar{r} = \bar{r}_{max} \geqslant 10. \tag{3.3}$$

At the cell mid-plane (boundary 3),

$$\bar{n} = 0, \quad \bar{\phi} = 0, \quad \bar{z} = H/2a, \tag{3.4}$$

since H is much larger than the particle size and the perturbation induced by the particle becomes negligible.

On the particle (boundary 5), the conditions are subtler. In the context of the linearized model, the charge flux vanishes,

$$2\nabla\bar{\phi} \cdot \boldsymbol{n} + \nabla\bar{n} \cdot \boldsymbol{n} = 0, \tag{3.5}$$

and the electric displacement is continuous,

$$\varepsilon\nabla\bar{\phi} \cdot \boldsymbol{n} - \varepsilon_p\nabla\bar{\phi}_p \cdot \boldsymbol{n} = 0. \tag{3.6}$$

Note that there is no bound charge in the latter expression because the oscillatory part of the bound charge vanishes. By restricting attention to situations where $\varepsilon \gg \varepsilon_p$, these boundary conditions reduce to

$$\nabla\bar{\phi} \cdot \boldsymbol{n} = 0, \quad \nabla\bar{n} \cdot \boldsymbol{n} = 0. \tag{3.7}$$

In the linearized model, the effects of electro-osmosis on charge transport inside the Debye layer are absent since the Péclet number vanishes. Effects due to particle charge and the attendant transport processes in the diffuse layer can be taken into account in an *ad hoc* fashion, however. A thin diffuse layer near a particle surface with a non-zero charge concentration gives rise to both a higher ionic conductivity and electro-osmotic flow. By extending the work of O'Konski (1960) and Dukhin & Shilov (1980), O'Brien (1986) showed that both effects can be captured under the rubric of 'surface conduction'. Thus, a current balance applied to a slab-shaped control volume on the particle surface yields the boundary condition

$$(K_e - i\varepsilon\varepsilon_0\omega)\nabla\phi \cdot \boldsymbol{n} - (K_p - i\varepsilon_p\varepsilon_0\omega)\nabla\phi_p \cdot \boldsymbol{n} = -K_s\nabla_s^2\phi, \quad r = a, \tag{3.8}$$

where K_e and K_p are the ionic conductivities of the fluid and particle, respectively, K_s is the particle 'surface conductivity', and ∇_s denotes the surface Laplacian. The terms on the left-hand side of the equation represent the normal current flux into the surface layer, while the term on the right-hand side represents the tangential current along the particle surface. The surface conductivity, K_s, depends on the Debye thickness and the amount of free charge in the double layer (or, equivalently, the surface potential) as embodied in, e.g. the Bikerman equation (Bikerman 1939),

$$K_s = \frac{K_e}{\kappa}\left(\exp\left|\frac{e\zeta_p}{2k_BT}\right| - 1\right)(1 + 3M_D). \tag{3.9}$$

Here, ζ_p is the particle surface potential and $M_D = 2\varepsilon\varepsilon_0(k_BT)^2/(3\mu e^2 D)$ is the dimensionless ionic drag coefficient.

Accordingly, with $\varepsilon_p \ll \varepsilon$,

$$\nabla\bar{\phi} \cdot \boldsymbol{n} = -\lambda\nabla_s^2\bar{\phi}, \quad \nabla\bar{n} \cdot \boldsymbol{n} = 0. \tag{3.10}$$

Here, $\lambda \equiv K_s/(K_e - i\varepsilon\varepsilon_0\omega)$ is the complex dimensionless surface conductivity and, with $\lambda = 0$, (3.10) describes behaviour without surface conduction.
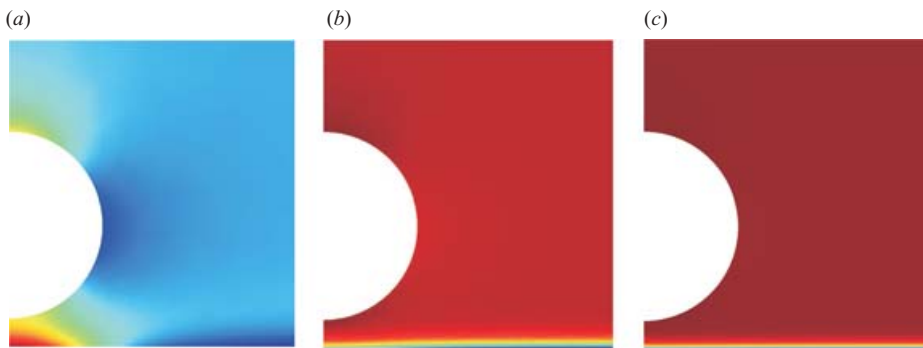
(a) (b) (c)

FIGURE 3. Relative magnitudes of the vertical component of the electric field strength calculated with the finite-element scheme (arbitrary colour scales) and the linearized model. (a) $\kappa^{-1} = 100$ nm; (b) $\kappa^{-1} = 33$ nm; (c) $\kappa^{-1} = 20$ nm. Parameters: $a = 500$ nm, $H = 200$ μm, $h = 150$ nm, $\lambda = 0$, $\omega = 1$ kHz, $D = 2 \times 10^{-9}$ m^2 s^{-1}.

3.3. *Numerical methodology*

Numerical calculations were carried out in Femlab version 3.0a (Comsol Software), using the direct (UMFPACK) stationary linear solver with the 'weak' solution form (for details, refer to chap. 6 of The Femlab User's Guide, Version 3.0). Complex-valued equations were divided into a system of two equations and solved independently. To check the accuracy of the methodology, four problems with known analytical solutions were solved: the dipole field around an isolated dielectric particle in an external field (Jackson 1975); the dipole field around an isolated particle with a surface conductivity (O'Brien 1986); the hydrodynamic mobility of a sphere moving toward a planar wall (Brenner 1961); and the coupled charge and electric potential between parallel electrodes (Hollingsworth & Saville 2003). Excellent agreement between the analytical solutions and the numerical results was readily obtained with relatively coarse meshes in the first three problems.

The accuracy of the numerical solution of the fourth problem (coupled charge and potential) is sensitive to the mesh parameters owing to the steep gradient at an electrode surface. Quite small elements were needed to obtain accurate results. To address this issue and deal with computer memory limitations, a variable mesh-size scheme was used wherein the size increased upon moving away from the electrode. However, even with a variable mesh, the large memory requirement limited the size of the domain analysed and restricted the numerical studies to situations where $\kappa a < 30$.

3.4. *Numerical results*

We focus here on frequencies $\omega \gg \kappa D/H$, such that far from the particle, the field strength outside of the polarization layer is approximately $\Delta\phi/2H$. The main conclusions in the following discussion also apply to lower frequencies, but the magnitude of the field strength at the edge of the polarization layer is correspondingly lower (cf. §2.2).

As expected, unless the Debye layer thickness is small, the particle distorts the electric field strength along the electrode; figure 3 shows relative magnitudes of the electric field for different values of a/κ^{-1}. The distortion decays quickly as a/κ^{-1} increases. In addition, the non-uniformity is localized underneath the particle and becomes negligible for $r/a > 2$. For Debye lengths such as those employed in the experimental work the distortion should be relatively minor.
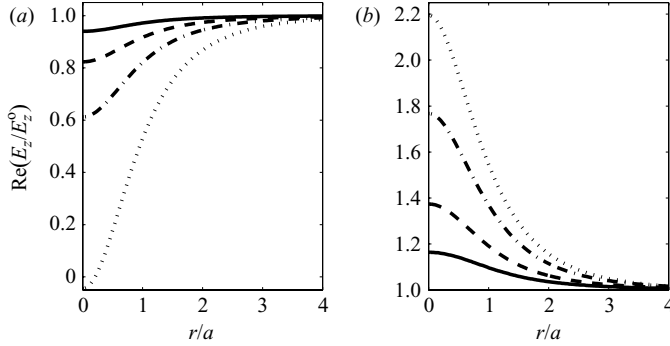
FIGURE 4. Numerical computations of the real part of the vertical electric field strength along the electrode ($z = 0$), normalized on the field strength in the absence of the particle, as a function of radial position. (a) A particle with zero surface conductivity. $\cdots$, $\kappa a = 5$, $\kappa h = 1.5$; $-\cdot-$, $\kappa a = 10$, $\kappa h = 3$; $---$, $\kappa a = 15$, $\kappa h = 4.5$; ——, $\kappa a = 25$, $\kappa h = 7.5$. (b) A particle with a high surface conductivity corresponding to $\zeta_p = -200\,\mathrm{mV}$. $\cdots$, $\kappa a = 10$, $\kappa h = 3$; $-\cdot-$, $\kappa a = 15$, $\kappa h = 4.5$; $---$, $\kappa a = 20$, $\kappa h = 6$; ——, $\kappa a = 25$, $\kappa h = 7.5$. The dimensionless surface conductivities are, respectively, $\lambda = 4.13 + 3.25i$, $3.97 + 1.39i$, $3.21 + 0.63i$, and $2.63 + 0.33i$. Parameters: $h/a = 0.3$, $\omega = 1\,\mathrm{kHz}$, $\varepsilon_p = 0$, $D = 2 \times 10^{-9}\,\mathrm{m^2\,s^{-1}}$.

A more quantitative comparison is presented in figure 4, which depicts the (numerically calculated) ratios of the field strengths at the electrode with and without the particle for different values of κa. For an uncharged particle (with zero surface conductivity) the electric field decreases beneath the particle (figure 4a). For a highly charged particle (high surface conductivity), the electric field strength increases under the particle (figure 4b). However, as the results demonstrate, the influence of the particle diminishes as a/κ^{-1} increases. For even smaller Debye lengths, e.g. $a/\kappa^{-1} \gg 50$, the distortion should be insignificant; in our experimental work $a/\kappa^{-1} \approx 5000$.

These results can be understood in terms of the dipole coefficient of an isolated particle. For an isolated particle with $\varepsilon_p \ll \varepsilon$, the dipole coefficient is

$$C_o = \frac{2\lambda - 1}{2\lambda + 2}. \tag{3.11}$$

Thus, for low-conductivity particles ($\lambda < 1/2$), the dipole coefficient is negative and the dipole field is oriented in the direction opposite to the applied field. For highly conducting particles ($\lambda > 1/2$) the dipole coefficient is positive, and the dipole field is aligned with the applied field. For $\lambda = 1/2$, the particle is effectively 'transparent' and the electric field is unaffected by the particle. Thus, when the particle is in the vicinity of an electrode, the dipole field of the particle 'competes' with the electric field just outside the electrode polarization layer. If the particle dipole coefficient is negative, the dipole field decreases the field strength underneath the particle. When the particle dipole coefficient is positive, the dipole field augments the field under the particle.

As indicated in figures 3 and 4, the magnitude of the distortion diminishes as the Debye length decreases. Decreasing the Debye thickness has two effects: (i) the polarization layer recedes from the particle; and (ii) the field strength in the polarization layer increases while the dipole field remains roughly constant. Both effects decrease the distortion due to the particle, showing that the field at the edge of the polarization layer becomes uniform as $\kappa^{-1} \to 0$. Accordingly, the particle 'sees' a uniform field above the nearby electrode and this can be used as an asymptotic boundary condition for thin polarization layers, thereby facilitating analytical treatment. This matter will
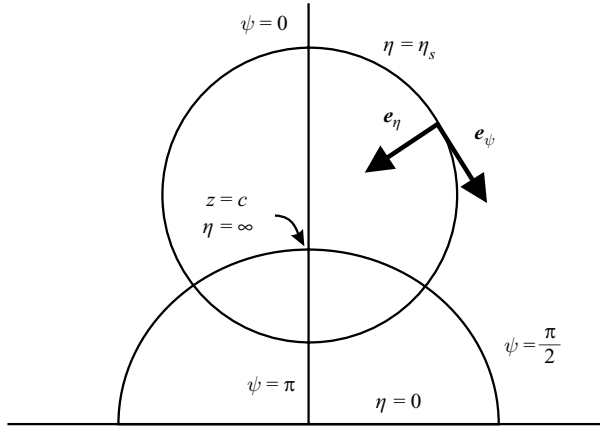
FIGURE 5. Definition sketch for the bispherical coordinate system.

be revisited in §5 in connection with a comparison between flow fields calculated numerically with the full model and with the asymptotic boundary conditions.

4. The electric potential around a particle with a thin-double layer

4.1. *Thin-double-layer formulation*

When the Debye length is small compared to the particle size ($\kappa a \gg 1$), polarization layers are thin and, since $\kappa a \sim 5000$ in the experiments to which the theory will be applied, this restriction is readily satisfied. When the free charge density is zero everywhere in the domain, the equation for the potential reduces to Laplace's equation,

$$\nabla^2 \phi = 0. \tag{4.1}$$

The boundary conditions for the problem are as follows. First, the influence of the particle decays at large distances so

$$\phi \to -E_\infty z, \quad z \to \infty, \tag{4.2}$$

where, for oscillatory fields, E_∞ follows from (2.12). On the particle surface, the current balance (cf. §3.2) relates the normal and tangential derivatives of the electric potential,

$$\varepsilon^* \nabla \phi \cdot \boldsymbol{n} - \varepsilon_p^* \nabla \phi_p \cdot \boldsymbol{n} = -K_s \nabla_s^2 \phi, \quad r = a. \tag{4.3}$$

On the electrode surface, the electric field strength is uniform along the edge of the infinitesimally thin polarization layer, cf. §3, so

$$\nabla \phi \cdot \boldsymbol{n} = -E_\infty, \quad z = 0. \tag{4.4}$$

4.2. *Bispherical coordinates and the particle position*

The bispherical coordinate system (Moon & Spencer 1988) is the natural choice to describe the domain since the boundary conditions (on the electrode and particle surface) correspond to coordinate surfaces (figure 5). Bispherical coordinates are related to Cartesian coordinates by the formulae

$$x = \frac{c \sin \psi \cos \theta}{\cosh \eta - \cos \psi}, \tag{4.5a}$$

$$y = \frac{c \sin \psi \sin \theta}{\cosh \eta - \cos \psi}, \tag{4.5b}$$

$$z = \frac{c \sinh \eta}{\cosh \eta - \cos \psi}, \tag{4.5c}$$

$$c = \sqrt{h^2 - a^2}, \tag{4.5d}$$

$$-\infty \leqslant \eta \leqslant \infty, \; 0 \leqslant \psi \leqslant \pi, \; 0 \leqslant \theta \leqslant 2\pi. \tag{4.5e}$$

Here surfaces of constant η are spheres, with radius $c|\operatorname{cosech}\eta|$ centred at $h = c \coth \eta$. An infinitely large sphere corresponds to $\eta = 0$, the plane between the two spheres. The particle surface corresponds to $\eta = \eta_s$, so $c = a \sinh \eta_s$, and $h = a \cosh \eta_s$. Surfaces of constant ψ are 'lemon' shaped for $\psi > \pi/2$ and 'apple' shaped for $\psi < \pi/2$. The vertical and radial vectors are related by

$$\boldsymbol{e}_r = \frac{\cos \psi \cosh \eta - 1}{\cosh \eta - \cos \psi} \boldsymbol{e}_\psi - \frac{\sin \psi \sinh \eta}{\cosh \eta - \cos \psi} \boldsymbol{e}_\eta, \tag{4.6}$$

$$\boldsymbol{e}_z = -\frac{\sin \psi \sinh \eta}{\cosh \eta - \cos \psi} \boldsymbol{e}_\psi + \frac{1 - \cos \psi \cosh \eta}{\cosh \eta - \cos \psi} \boldsymbol{e}_\eta. \tag{4.7}$$

The bispherical parameter c follows from the particle height above the electrode.

In bispherical coordinates,

$$\nabla_s^2 \phi = \frac{(\cosh \eta - \cos \psi)^2}{c^2 \sin \psi} \frac{\partial}{\partial \psi} \left(\sin \psi \frac{\partial \phi}{\partial \psi} \right). \tag{4.8}$$

Since $\varepsilon_p \ll \varepsilon$ for typical systems (e.g. polystyrene or silica in water),

$$\frac{\partial \phi}{\partial \eta} = \lambda \frac{(\cosh \eta - \cos \psi)}{\sinh \eta \sin \psi} \frac{\partial}{\partial \psi} \left(\sin \psi \frac{\partial \phi}{\partial \psi} \right), \quad \eta = \eta_s, \tag{4.9}$$

where λ is the dimensionless (complex) conductivity introduced earlier, cf. (3.10).

The solution to Laplace's equation in bispherical coordinates that satisfies the far-field boundary condition is (Moon & Spencer 1988)

$$\phi = -z + \sinh \eta_s (\cosh \eta - \xi)^{1/2} \sum_{n=0}^{\infty} (A_n \cosh(n + 1/2)\eta + B_n \sinh(n + 1/2)\eta) \mathscr{P}_n(\xi), \tag{4.10}$$

with ϕ and z scaled with $a E_\infty$ and a, respectively, P_n is the Legendre polynomial of degree n, and $\xi \equiv \cos \psi$. The constant field strength boundary condition at $\eta = 0$ requires

$$B_n = 0. \tag{4.11}$$

To determine the A_n coefficients, we follow Morrison & Stukel (1970) and use the orthogonality relations for Legendre polynomials in integral form. The result is a ninth-order recursion relation; truncation of the infinite series at $m = N_{tot}$ yields a matrix equation of the form

$$(\boldsymbol{M}_\eta - \lambda \boldsymbol{M}_\psi) \cdot \boldsymbol{A} = \boldsymbol{I}_\eta - \lambda \boldsymbol{I}_\psi, \tag{4.12}$$

where $\boldsymbol{A} = \{A_0, A_1, A_2, \ldots, A_{N_{tot}}\}$ is the desired vector of coefficients. The vectors $\boldsymbol{I}_\eta$ and $\boldsymbol{I}_\psi$ stem from integration of the normal and surface derivatives, respectively, of the unperturbed electric field (the first term in (4.10)). Likewise, the elements of the heptadiagonal matrix $\boldsymbol{M}_\eta$ and the nonadiagonal matrix $\boldsymbol{M}_\psi$ result from integration of the normal and surface derivatives of the perturbed electric field (the second term in (4.10)). All four are lengthy expressions involving m and η_s, but the A_m coefficients are readily calculated by standard numerical methods (Ristenpart 2005).
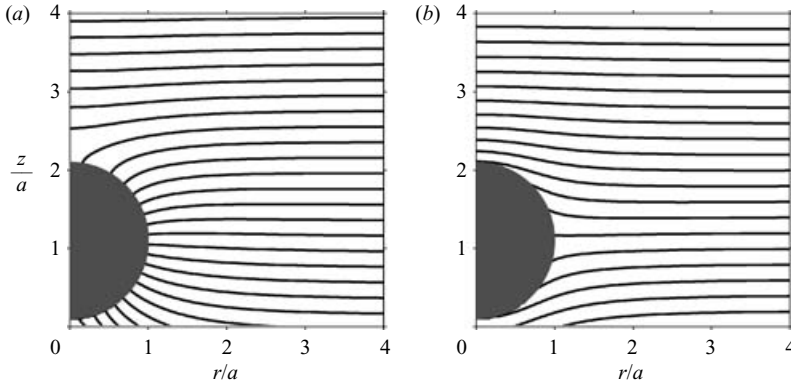
FIGURE 6. The electric potential around a particle near an electrode subject to a uniform field strength at time $t = n/2\pi\omega$. The particle is located at $h/a = 0.1$. (a) $\lambda = 0$, equivalent dipole strength $C_0 = -0.5$. On the electrode surface, the potential decreases radially. (b) $\lambda = 1.34 + 0.03i$, equivalent dipole strength $C_0 = 0.36 + 0.01i$. On the electrode surface, the potential increases radially.

4.3. *Results for the potential*

The **M** matrices and **I** vectors were tabulated with Mathematica and (4.12) was solved with the LinearSolve function. Complex-valued equations were divided into a system of two equations and solved independently. For the work discussed here, the series converged for values of N_{tot} between 50 and 600, depending on the value of η_s. The results were confirmed independently by a finite-element approach (Femlab).

Figure 6 shows representative results. For a particle with zero surface conductivity, the equipotential lines are similar to those for an isolated insulating particle, although the presence of the electrode clearly distorts the field (figure 6a). Notably, the condition of constant field strength on the electrode results in a non-uniform potential underneath the particle. For a particle with low or zero surface conductivity, the gradient in potential along the electrode is directed away from the particle. For particles with a higher surface conductivity (figure 6b), the situation is reversed and the equipotential lines are similar to those for an isolated conducting particle. Underneath the particle, the potential gradient is directed toward the particle.

5. Fluid flow around a particle

5.1. *Formulation and streamfunctions*

Since inertial effects are negligible and free charge is confined to thin regions near solid surfaces, the momentum balance and continuity equation are

$$\mathbf{0} = -\nabla P + \nabla^2 \mathbf{u}, \quad \nabla \cdot \mathbf{u} = 0. \tag{5.1}$$

For boundary conditions, we first specify that the velocity normal to every solid surface is zero,

$$\mathbf{u} \cdot \mathbf{n} = 0, \quad r = a, \quad z = 0. \tag{5.2}$$

For the tangential velocities, we employ the standard electro-osmotic slip condition. As discussed by Squires & Bazant (2004), a perturbation expansion of the standard

model near a conducting surface yields the velocity components

$$u_t = -\frac{\varepsilon\varepsilon_0\phi E_t}{\mu}(1 - e^{-\kappa z}) + O\left(\frac{1}{\kappa\ell}\right), \quad u_z = O\left(\frac{1}{\kappa\ell}\right). \tag{5.3}$$

Here, ϕ and E_t are the potential and tangential electric field induced by the applied field at the outer edge of the diffuse layer, z is the coordinate in the direction normal to a surface, and ℓ is a characteristic length. (For convenience the reference state for the potential may be shifted such that the potential is zero at the electrode, so that ϕ in (5.3) is equivalent to the potential drop across the charged layer.) Thus, to leading order, the normal velocity is zero and the slip velocity is as given by the Smoluchowski equation. To relate the velocity to the surface potential gradient and the charge in a polarization layer, we use Gauss' law to obtain

$$u_t = \frac{\varepsilon\varepsilon_0\phi E_t}{\mu} = \frac{q E_t}{\mu\kappa}; \tag{5.4}$$

q denotes the free charge density. In general, the charge on the particle or electrode is composed of two terms: 'equilibrium' charge present in the absence of a field, and charge induced by the applied field, namely,

$$q(t) = q_{eq} + q_{ind}(t). \tag{5.5}$$

Since the applied field varies as $\cos\omega t$, the flow resulting from the equilibrium charge simply oscillates as $\cos\omega t$. Flow resulting from the induced charge, however, oscillates as $\cos^2\omega t = (1 + \cos 2\omega t)/2$, and thus has both a 'steady' component and a component that fluctuates at twice the imposed frequency. Focusing on the steady (rectified) part of the velocity field enables us to omit the flow arising from the action of the oscillatory field on fixed charges.

Charge is induced on both the particle surface and the electrode, but the following argument shows that slip velocity on the electrode dominates. On the electrode, the induced charge is (cf. §2.2)

$$q \sim \varepsilon\varepsilon_0 E_\infty(1 + i\kappa^2 D/\omega)e^{-i\omega t}, \tag{5.6}$$

and the induced charge along the particle surface is, from Gauss' law and (3.8),

$$q \sim \varepsilon\varepsilon_0 E_\infty \lambda a\nabla_s^2\phi e^{-i\omega t}. \tag{5.7}$$

To estimate the tangential electric field on the electrode, the point dipole estimate $E_t \sim C_0 E_\infty$ evaluated at $r \sim a$ and $h \sim 0$ can be used. On the particle surface, the surface Laplacian is $\nabla_s^2\phi \sim E_\infty/a$ so $E_t \sim E_\infty$. These estimates indicate that the velocity induced on the particle surface is negligible compared to that along the electrode if

$$C_0(1 + i\kappa^2 D/\omega) \gg \lambda. \tag{5.8}$$

Inasmuch as $C_0 \sim (2\lambda - 1)/(2\lambda + 2)$ and $\kappa^2 D \gg \omega$, this restriction is easily satisfied. Thus, on the particle surface we specify

$$\boldsymbol{u} \cdot \boldsymbol{t} = 0, \quad r = a. \tag{5.9}$$

We emphasize that (5.6) is an approximation for the charge density because, similar to the constant-field strength boundary condition employed previously, it neglects the presence of the particle. To be strictly consistent in the context of the constant field strength condition (4.4), one might consider employing Gauss' law to obtain a charge density that is without the second term in (5.6). For frequencies $\omega \ll \kappa^2 D$, this approach neglects the dominant term, however, and the resulting flow predictions are

inconsistent with the numerical solution to the complete electrokinetic model. As we shall see, use of (5.6) for the charge density yields excellent agreement (cf. figure 8).

The axisymmetric nature of the problem allows us to employ a streamfunction, Ψ, defined by

$$u_\eta = \frac{(\cosh \eta - \cos \psi)^2}{c^2 \sin \psi} \frac{\partial \Psi}{\partial \psi}, \tag{5.10}$$

$$u_\psi = -\frac{(\cosh \eta - \cos \psi)^2}{c^2 \sin \psi} \frac{\partial \Psi}{\partial \eta}. \tag{5.11}$$

The general solution of Stokes' equations in bispherical coordinates is (Stimson & Jeffery 1926)

$$\Psi = (\cosh \eta - \cos \psi)^{-3/2} \sum_{n=1}^{\infty} W_n(\eta) G_{n+1}^{-1/2}(\cos \psi), \tag{5.12}$$

where

$$W_n(\eta) = a_n \cosh[(n - 1/2)\eta] + b_n \sinh[(n - 1/2)\eta] + c_n \cosh[(n + 3/2)\eta] \\ + d_n \sinh[(n + 3/2)\eta], \tag{5.13}$$

and $G_{n+1}^{-1/2}(\cos \psi)$ is the Gegenbauer polynomial of order $n+1$ and degree $-1/2$, given by

$$G_{n+1}^{-1/2}(\cos \psi) = \frac{P_{n-1}(\cos \psi) - P_{n+1}(\cos \psi)}{2n + 1}. \tag{5.14}$$

It now remains to use the boundary conditions on the particle and electrode surfaces to determine the unknown coefficients. The condition of no normal flow at the electrode and particle surfaces indicates that $\Psi = 0$ at both $\eta = 0$ and $\eta = \eta_s$, yielding

$$a_n = -c_n, \tag{5.15}$$

and

$$a_n \cosh[(n - 1/2)\eta_s] + b_n \sinh[(n - 1/2)\eta_s] \\ + c_n \cosh[(n + 3/2)\eta_s] + d_n \sinh[(n + 3/2)\eta_s] = 0. \tag{5.16}$$

Since the slip velocity along the particle surface is negligible,

$$u_t = 0 \rightarrow \frac{\partial \Psi}{\partial \eta} = 0, \quad \eta = \eta_s, \tag{5.17}$$

which yields

$$a_n(n - 1/2) \sinh[(n - 1/2)\eta_s] + b_n(n - 1/2) \cosh[(n - 1/2)\eta_s] \\ + c_n(n + 3/2) \sinh[(n + 3/2)\eta_s] + d_n(n + 3/2) \cosh[(n + 3/2)\eta_s] = 0. \tag{5.18}$$

To specify the charge induced on the electrode, we combine (2.12) and (5.6), which imply that the perturbation caused by the particle is negligible compared to the influence of the applied field, as confirmed numerically in the limit as $\kappa^{-1} \rightarrow 0$ (cf. §3). The electro-osmotic slip velocity along the electrode (at $\eta = 0$) is thus

$$\frac{(\cosh \eta - \cos \psi)^2}{c^2 \sin \psi} \frac{\partial \Psi}{\partial \psi} = \frac{\varepsilon \varepsilon_0 E_\infty}{\mu \kappa} \left(1 + i\frac{\kappa^2 D}{\omega}\right) \frac{(\cosh \eta - \cos \psi)}{c} \frac{\partial \phi}{\partial \psi}, \tag{5.19}$$

where the dimensionless potential ϕ is specified by the solution obtained in the previous section. Defining the scaling factor

$$\Psi \to \frac{\varepsilon \varepsilon_0 c^2 E_\infty^2}{\mu \kappa} \Psi, \tag{5.20}$$

and noting that the streamfunction is zero on the electrode yields

$$\sum_{n=1}^\infty \frac{\mathrm{d} W_n}{\mathrm{d} \eta} G_{n+1}^{-1/2}(\xi) = (1-\xi^2)(1-\xi)^{1/2} \left(1 + \mathrm{i} \frac{\kappa^2 D}{\omega}\right) \frac{\partial \phi}{\partial \xi}, \tag{5.21}$$

where $\xi \equiv \cos \psi$. Integrating over ξ, and making use of orthogonality relations (5.15), (5.16) and (5.18) yields a matrix expression of the form

$$\boldsymbol{M}_\Psi \cdot \boldsymbol{b} = \boldsymbol{I}_\phi. \tag{5.22}$$

Here, $\boldsymbol{b} = \{b_1, b_2, \ldots, b_{N_{tot}-2}\}$ is the desired vector of coefficients, the mth element of the vector $\boldsymbol{I}_\phi$ is defined by

$$\boldsymbol{I}_\phi(m) = -A_{m-2} \frac{m(m-1)}{2(2m-1)} + A_{m-1} \frac{m(m-1)}{(2m-1)} + A_m \frac{2m^2 + 2m - 1}{(2m-1)(2m+3)}$$
$$- A_{m+1} \frac{(m+1)(m+2)}{(2m+3)} + A_{m+2} \frac{(m+1)(m+2)}{2(2m+3)}, \tag{5.23}$$

and the bidiagonal matrix $\boldsymbol{M}_\Psi$ is defined by the expressions

$$\boldsymbol{M}_\Psi(m-1) = -\frac{m-3/2}{2m-1} - \frac{m+1/2}{2m-1}\left(\frac{2m-3-(2m-1)\cosh 2\eta_s + 2\cosh[-(2m-1)\eta_s]}{2m+1-(2m-1)\cosh 2\eta_s - 2\cosh[-(2m-1)\eta_s]}\right),$$
$$\boldsymbol{M}_\Psi(m+1) = \frac{m+1/2}{2m+3} + \frac{m+5/2}{2m+3}\left(\frac{2m+1-(2m+3)\cosh 2\eta_s + 2\cosh[(2m+3)\eta_s]}{2m+5-(2m+3)\cosh 2\eta_s - 2\cosh[(2m+3)\eta_s]}\right). \tag{5.24}$$

Note that the A_m coefficients are those obtained from (4.12), and the infinite series was truncated at $m = N_{tot} - 2$.

5.2. *EHD flow in oscillatory fields*

Equation (5.22) was solved using a procedure similar to that described for (4.12), i.e. the LinearSolve function in Mathematica and independent corroboration in Femlab. Representative EHD streamlines are presented in figure 7 for a particle located at $h/a = 0.1$. The flow structure is toroidal, with the recirculation centred under the particle edge ($z/a \sim 0.25$). The velocity increases rapidly underneath the particle, before rapidly changing direction and moving away from the particle.

The direction of the flow depends on the particle surface conductivity. For particles with low surface conductivity (cf. figure 10) the flow along the electrode is directed toward the particle. This result is expected from consideration of the potential gradients presented in figure 6. For an uncharged particle at time $t = n/2\pi\omega$, the potential decreases radially along the electrode. The radial electric field $E_r = -\nabla_r \phi$ is thus directed away from the particle. At $t = n/2\pi\omega$, the ions near the electrode are negatively charged, and thus the radial electric field exerts a body force directed toward the particle. Although the electric field and charge distribution oscillate in time, the steady component of the body force remains oriented toward the particle. For highly conducting particles, the potential gradient is reversed and flow is directed away from the particle.
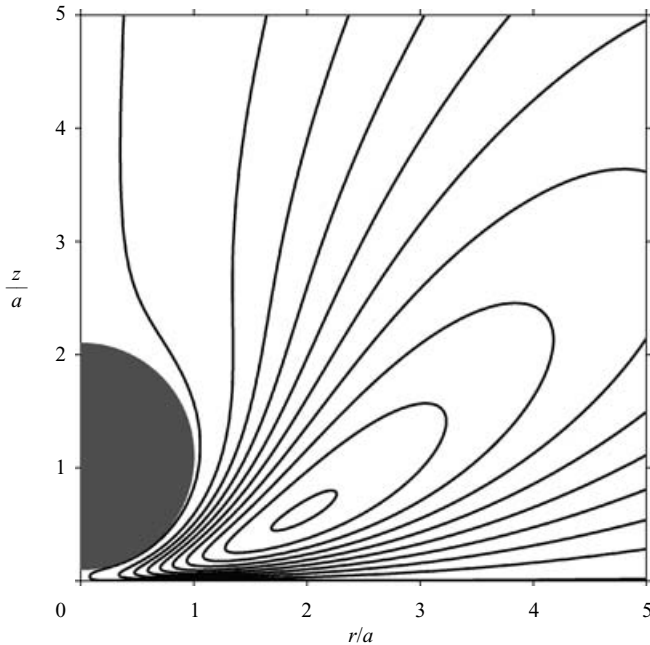
FIGURE 7. Streamlines for EHD flow. The flow direction is clockwise for $C_o' < 0$ and counterclockwise for $C_o' > 0$. The particle height is $h/a = 0.1$.

For comparison, numerical solutions of the Stokes equations with an electric body force (2.1) were carried out. Here the electric body force was extracted from the numerical solutions for the potential and charge density discussed in §4. No-slip conditions were applied on the electrode and particle surfaces, while a symmetry condition was employed along the left-hand vertical boundary (near the particle). Either a no-slip or a symmetry boundary condition was applied along the right-hand-side vertical boundary; the different conditions yielded little difference in the fluid velocity near the particle, provided the domain width was sufficiently large.

A representative plot of the radial EHD velocity along the particle centreline is shown in figure 8 for an uncharged particle with $\kappa a = 20$. Flow is directed radially inward far from the particle surface (negative velocities), while close to the surface the recirculating fluid is directed radially outward (positive velocities). The key result is that the velocities obtained with the full numerical solution with a constant potential boundary condition (cf. §3) are in excellent agreement with the asymptotic solution. The qualitative aspects of the flow around the particle calculated by either method are the same; for $\kappa a > 20$, the streamlines around the particle (outside of the polarization layer) calculated numerically are almost indistinguishable from those calculated analytically. Although the magnitudes of the velocities differ, the difference decreases as κa increases. A simple extrapolation of the ratio between the 'exact' numerical solution and the approximate analytical solution indicates that the ratio rapidly approaches unity as κa increases (figure 8, inset). That the numerically calculated velocities approach those of the thin-double-layer model further supports the use of the constant-field-strength boundary condition.

Besides the electric field conditions, two other parameters affect the EHD velocity: the particle height above the electrode and the surface conductivity. As the particle moves closer to the electrode, the magnitude of the EHD velocity increases
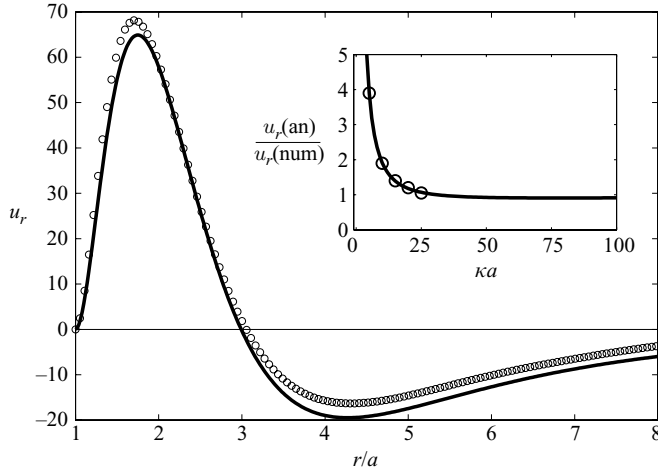
FIGURE 8. Comparison of radial velocities calculated numerically and analytically. ○, numerical solution with a volumetric body force; ——, analytical solution with slip conditions specified at the boundaries. Velocities in $\mu\mathrm{m\,s}^{-1}$, evaluated at $z/a = 1.3$; negative values indicate the flow is directed radially inward toward the particle. Particle located at $h/a = 0.3$, and $\kappa^{-1} = 20\,\mathrm{nm}$. Inset: ratio of the analytically calculated velocity to the numerical one as a function of Debye thickness, calculated at $r/a = 2$. ○, computed value; ——, polynomial fit. As the Debye thickness diminishes, the two calculations converge. $\omega = 1\,\mathrm{kHz}$, $E = 5\,\mathrm{V\,cm}^{-1}$, $K_s = 0$, $D = 2 \times 10^{-9}\,\mathrm{m}^2\,\mathrm{s}^{-1}$.
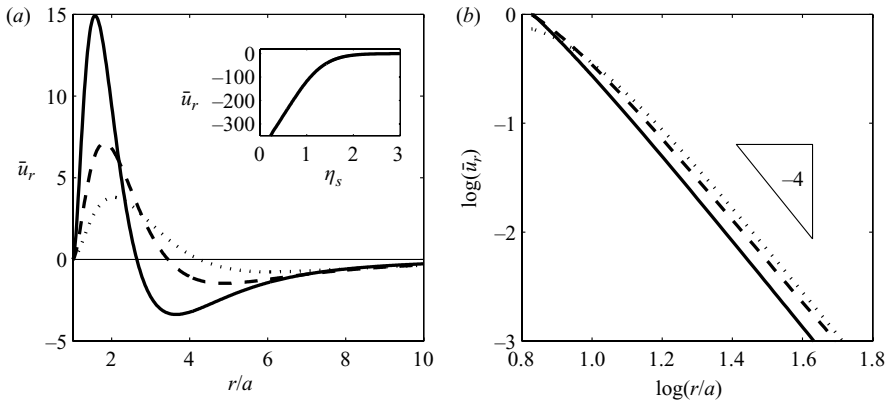

FIGURE 9. (*a*) Radial (dimensionless) EHD velocity–radial position relation at the particle mid-plane for different particle–electrode separations. $\cdots$, $h/a = 1$; $---$, $h/a = 0.5$; ——, $h/a = 0.01$. Inset: The radial velocity at $z/a = 0$, $r/a = 1$ as a function of η_s. (*b*) Log–log plot of the radial velocity–radial position for $r/a > 5$, evaluated at the same particle heights as in (*a*). The flows decay as r^{-4} far from the particle, $\kappa^{-1} = 10\,\mathrm{nm}$, $\omega = 1\,\mathrm{kHz}$, $D = 2 \times 10^{-9}\,\mathrm{m}^2\,\mathrm{s}^{-1}$.

dramatically (figure 9*a*). For particles far from the electrode, the velocity is effectively zero, but it increases roughly linearly with η_s (exponentially as h/a). The velocity diverges as the separation approaches zero, but in practice the particles are separated from the electrode by colloidal forces (cf. §6.2).

Far from the particle, the radial velocity decays as r^{-4} (figure 9*b*). This scaling can be understood in terms of the reflection of a 'phoretic' flow off the electrode. As opposed to forced flows that decay as r^{-1} (e.g. sedimentation), phoretic flows (e.g. particle electrophoresis) are driven by the interaction of an external field on a surface
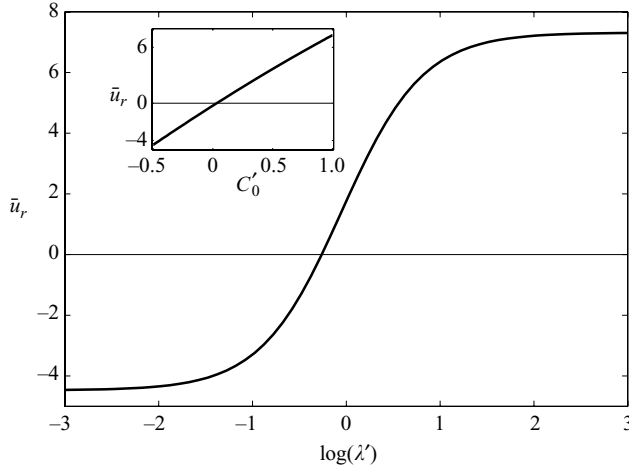
FIGURE 10. Normalized radial EHD velocity as a function of the real component of the normalized particle surface conductivity. Velocities calculated at a representative position slightly above the particle ($r/a = 4$, $z/a = 1.05$) for a particle located at $h/a = 0.05$. The velocity decreases as the surface conductivity increases, eventually changing direction above a critical value. Inset: the same data plotted as a function of the real component of the dipole coefficient, $C_0 = (2\lambda - 1)/(2\lambda + 2)$, demonstrating the roughly linear dependence. $\kappa^{-1} = 10$ nm, $\omega = 1$ kHz, $D = 2 \times 10^{-9}$ m^2 s^{-1}.

within the fluid (Anderson 1989). Phoretic flows are of shorter range, decaying as r^{-3}. To incorporate the effect of an adjacent wall, one can use the method of reflections to show that to leading order, the radial velocity parallel to the wall is diminished by a factor of r^{-1} (Happel & Brenner 1973). Thus, the radial flow near a sedimenting particle decays as r^{-2}, while the radial flow near a particle undergoing electrophoretic deposition decays as r^{-4}. Although the EHD flows considered here do not strictly meet the criteria for 'phoretic' flows as set forth by Anderson (1989), they clearly share the key attribute of flow generated by slip along the domain boundaries.

The velocity magnitude and spatial structure are significantly affected by the particle position, but the direction of the flow is not. In contrast, both the magnitude and the direction (but not the structure) of the EHD flow are strongly dependent on the particle surface conductivity (figure 10). As the surface conductivity increases, the EHD flow diminishes in magnitude and eventually reverses sign to produce an outward flow. In terms of the dipole coefficient (3.11), the velocity increases linearly with C_o (figure 10, inset). At a critical surface conductivity (or corresponding dipole coefficient) the flow reverses direction.

This reversal has important implications in the aggregation of suspensions. If flow is directed radially inward, adjacent particles become mutually entrained in their respective flows and aggregate; they repel if the flow is directed radially outward. Even more complicated behaviour is expected in suspensions containing more than one type of particle. For example, a binary suspension of low and high conductivity particles will have three types of interaction: attraction between low conductivity particles; repulsion between high conductivity particles; and an intermediate interaction between unlike particles. Novel patterns are indeed observed with binary suspensions (Ristenpart, Aksay & Saville 2003), but dipolar interactions also play a critical role so it is difficult to isolate the effect of dipole coefficient on the fluid motion.

6. Particle tracking experiments

6.1. *Experimental approach, apparatus and methodology*

Flow-visualization near micrometre and submicrometre particles is difficult owing to Brownian motion. Moreover, tracer particles must be significantly smaller than a 'target' particle to provide authentic tracking; optical techniques are limited to particles larger than ~250 nm. Accordingly, it was decided to image the EHD flow near a large (>10 μm) particle with small (~300 nm) tracers. Large particles do not move significantly by Brownian motion and submicrometre tracer particles readily track fluid motion.

Particle-tracking experiments involved a cell with two parallel electrodes separated by a 250 μm polydimethylsiloxane (PDMS) spacer. The upper glass electrode was coated with a thin coating of indium tin oxide, an optically transparent semiconductor (Delta Technologies, $R_s = 4\Omega$). The lower electrode was a silicon slab coated with a 150 nm thick layer of platinum (Radiant Technologies). Prior to each experiment, the electrodes and spacer were cleaned by sonication in RBS-35 detergent (Pierce Chemicals), rinsed, sonicated again for 10 min in deionized water, and then dried with filtered nitrogen gas. Fluorescent tracer particles (300 nm diameter, Duke Scientific) were washed and diluted in 1 mM potassium chloride (KCl) to a volume fraction of approximately 10^{-3}. Flow was tracked around either 50 μm diameter silica or polystyrene particles (Duke Scientific).

To begin an experiment, an aliquot of the target particle suspension was placed in the cell, followed by a small amount of the tracer particle suspension. After the system became quiescent, oscillatory fields were applied with a Tektronix function generator (PFG5505) and measured with a Tektronix digital oscilloscope (TDS2012). Tracer particle motion in the EHD flow was observed through a Zeiss Axiovision fluorescence optical microscope and recorded with digital CCD camera. Images obtained in this fashion were oriented such that the electric field was directed normal to the plane of the image. Although the tracer particles are charged, electrophoretic motion is negligible in the high-frequency fields used here. The positions of the tracer particles were extracted from the recorded images using standard image analysis techniques.

6.2. *Results and comparison with theory*

When placed in the cell, the large target particles settled towards the bottom electrode where they remained effectively stationary. The 'resting height' of a particle depends on the balance between gravity, van der Waals attraction, electrostatic repulsion, steric forces and hydrodynamic drag. Fagan *et al.* (2002) showed that the equilibrium particle height for polystyrene particles is several Debye thicknesses and can change significantly in a strong electric field (presumably due to the drag force generated by EHD flow). The 50 μm silica particles employed in this work are much larger and denser, so gravity predominates over drag. The potential energies due to electrostatic repulsion (calculated using the Deraguin approximation), van der Waals attraction and gravity, are, respectively,

$$\Phi_{\mathrm{es}}(h) = 64\pi\varepsilon\varepsilon_0(k_B T/e)^2 \tanh(e\zeta_e/4k_B T)\tanh(e\zeta_p/4k_B T)\exp(-\kappa h), \qquad (6.1)$$

$$\Phi_{\mathrm{vdw}}(h) = -A\frac{a}{6h}\left[1 + \frac{h}{2a+h} + \frac{h}{a}\ln\left(\frac{h}{2a+h}\right)\right], \qquad (6.2)$$

$$\Phi_{\mathrm{g}}(h) = -4/3\pi a^3(\rho_s - \rho_f)gh. \qquad (6.3)$$

Here, A is the effective Hamaker constant for the particle and electrode; for platinum and silica immersed in water $A \sim 2.0 \times 10^{-20}$ J. The surface potentials of the electrode

and particle are ζ_e and ζ_p, respectively. For oscillatory fields, these values oscillate with the applied field, so even in the absence of electrokinetic effects the particle height varies. For frequencies $\omega \gg 100\,\text{Hz}$, however, the particle has insufficient time to move before the field changes direction (Fagan *et al.* 2002). Furthermore, for surface potentials much larger than $4\,k_B T/e$ the repulsive force is 'saturated', i.e. independent of the precise value. Assuming this to be the case for both surfaces yields a potential energy minimum at $h = 46\,\text{nm}$ ($h/a = 0.001$). The equation also indicates a large maximum at $h = 0.6$, but this small separation is outside the range for which the equation is valid. Nevertheless, this calculation and the flow visualization to be discussed shortly indicate that the target particle is separated from the electrode.

According to the Stokes–Einstein equation – with a logarithmic correction for the proximity of the electrode surface (Russel *et al.* 1991) – the time to migrate a certain distance is

$$t = \frac{6\pi\mu a \langle \boldsymbol{x}^2 \rangle}{2 k_B T} |\ln(h/a - 1)|. \tag{6.4}$$

Thus, a $50\,\mu\text{m}$ particle resident $50\,\text{nm}$ above the electrode requires $\sim 11\,\text{h}$ to move $5\,\mu\text{m}$ and Brownian motion of the target particles was negligible. To determine whether target particles were caught on the electrode, the cell was briefly tilted to a $\sim 30°$ angle. Target particles always moved immediately, consistent with a thin layer of liquid separating the particle from the electrode. Moreover, some small fraction of the target particles contained visible non-uniformities (bumps or blemishes). These non-uniformities did not rotate as the particles moved along the electrode, consistent with a sliding rather than rolling motion.

After visual confirmation that target particles were isolated, tracer particles were introduced into the cell. Tracers exhibited vigorous Brownian motion with no obvious bias, and upon application of the field, tracers close to a target began to move rapidly toward the target. No motion was apparent at potentials below $2\,\text{V}$ or at frequencies above $3\,\text{kHz}$. Directed tracer motion was clearly evident at locations between 1 and 2 target particle radii (50 to $100\,\mu\text{m}$) from the target particle (figure 11). A tracer's speed increased as it approached the target and disappeared from view underneath. Shifting the microscope focal plane half-way up the target particle ($\sim 50\,\mu\text{m}$) revealed tracer particles reappearing, although the motion was not easily discernible since the tracers moved almost vertically through the focal plane. Careful observation showed that the tracers were moving upward and away from the target. The outward motion was observed only near (within $\sim 50\,\mu\text{m}$) the edge of the particle and the speed was roughly a half to a quarter of the tracer velocity across the electrode. Moving the focal plane well above the target particle (100–$200\,\mu\text{m}$) revealed only Brownian motion.

Since polystyrene target particles are opaque, tracers are not observable underneath them. However, silica particles are transparent to visible light. Consequently, in reflection-mode microscopy, objects directly beneath a $50\,\mu\text{m}$ silica particle are visible, although their size is magnified by a factor of roughly two. Shifting the nominal focal plane below the bottom of the particle (to $\sim 10\,\mu\text{m}$ below the electrode) revealed tracer particles moving rapidly toward the 'south pole' of the target. When tracers were approximately 5 to $10\,\mu\text{m}$ away from the 'pole', they suddenly reversed direction. Such behaviour shows that dielectrophoretic forces are negligible since particles undergoing dielectrophoresis do not move into and then out of regions of high electric field strength (Pohl 1967).

In summary, observations were made with over a hundred target particles in different experimental cells. Tracers move primarily by Brownian motion until they
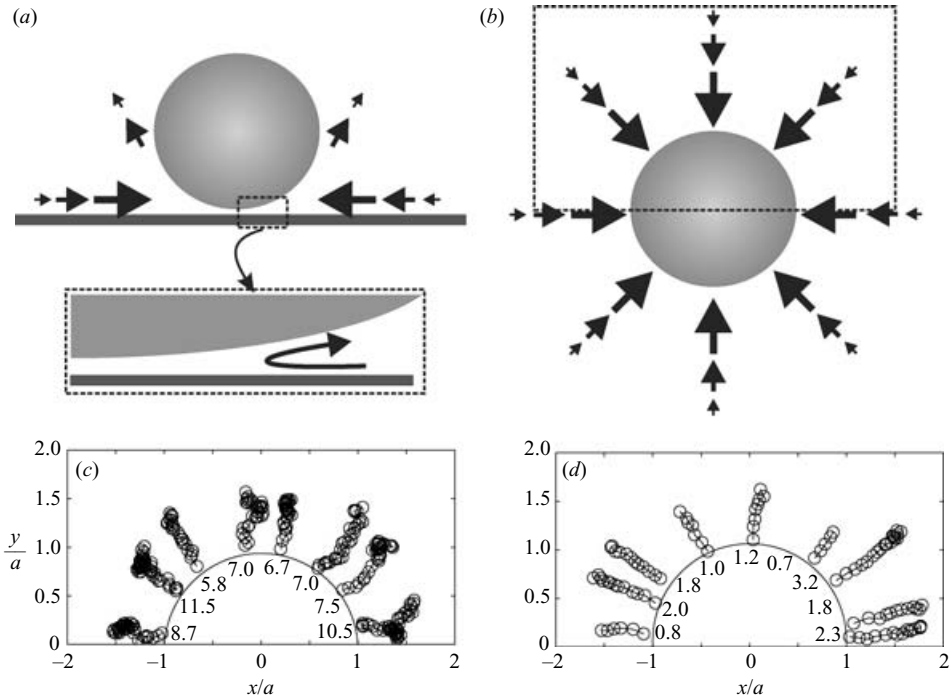
FIGURE 11. Particle-tracking results. Fluorescence microscopy was used to track 300 nm fluorescent polystyrene 'tracer' particles approaching a 50 μm silica target particle in an oscillatory electric field. (*a*) Cross-sectional schematic of tracer trajectories. The sudden change of direction was observed directly through a transparent silica particle. (*b*) Plan view of particle paths in a focal plane near the electrode. The rectangular box indicates the field-of-view. (*c*, *d*) Sequences of tracer positions as they approach the target particle near the electrode surface in a 750 Hz field: (*c*) $\Delta\phi = 4$ V and (*d*) $\Delta\phi = 9$ V. The semicircle indicates the outer diameter of the target particle, only half of which was within the microscope field-of-view during an experiment. The time intervals, in seconds, between the first appearance of the tracer particle in the focal plane and its disappearance underneath the target particle are noted adjacent to each trajectory. Note that Brownian motion affects the tracer trajectories at 4 V, but is less pronounced at 9 V.

are approximately 50 μm from the edge of the target particle, whereupon they begin to move radially inward, accelerating as they go. Underneath the target particle, tracers reverse course upon reaching a certain position, whereupon they move up and away from the target particle, slowing down as they move. The tracer particle motion accords with the streamlines presented in figure 7.

To provide more data to test the theoretical model, several dozen tracer particles were tracked as they moved towards an isolated silica particle (cf. figure 11*c*, *d*). Figure 12 shows radial positions at different potentials and frequencies. The time t_0 is defined as the time at which the tracers nominally reached the edge of the target particle. Owing to the finite acquisition rate of the CCD camera (1 image per ∼200 ms), the exact moment at which a particle disappears could not always be captured. To circumvent this problem, the time data for each tracer were normalized such that the tracer passed $r/a = 1.15$ at the same time; the time t_0 that best yielded the intercept for $r/a = 1$ was then determined. Although Brownian motion affected the trajectories, particularly at lower applied potentials or higher frequencies, the 'mean' trajectories were clearly delineated.
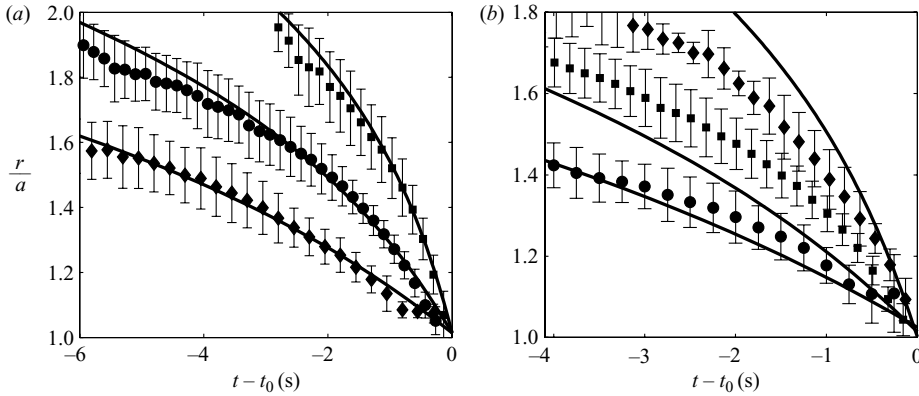
FIGURE 12. Radial positions of 300 nm fluorescent tracer particles moving across the electrode toward a 50 μm silica target particle as a function of time. The time, t_0, was defined as the time when the tracer particle moved under the edge of the target particle ($r/a = 1$). (*a*) Constant frequency (750 Hz) experiments at different applied potentials. ◆, 4 V; ●, 6 V; ■, 9 V. The number of tracer particles observed at each potential was 32, 22 and 28. Solid lines are the model predictions, using a surface conductivity, K_s, of 1.4 nS. (*b*) Constant potential ($\Delta\phi = 6$ V) experiments at different frequencies: ◆, 500 Hz; ■, 1000 Hz; ●, 1500 Hz. The number of tracer particles observed at each frequency was 19, 218 and 28. Solid lines are the model predictions, fit using the same surface conductivity, $K_s = 1.4$ nS.

The sizes of the error bars in figure 12 (one standard deviation in tracer position) are partly due to the obscuring effect of Brownian motion. Tracking over 200 tracers (rather than the typical 20) yielded little improvement (figure 12*b*, ■). Several effects contribute to the variability. First, the depth of the focal plane was approximately 6 μm, which limited the accuracy in determining the vertical location of a tracer with respect to the electrode. That some tracer particles moved noticeably faster or slower than others could be due to differences in their vertical location. Furthermore, some of the tracer paths appear to intersect the target particle at angles other than 90°, indicating non-axisymmetric flow. This is partly due to Brownian motion, as depicted in figure 11(*c*). Other factors are inhomogeneities on the particle or electrode surface and small displacements of the target particle.

To compare experiment and theory, the separation distances between the target particle and the electrode and that between the tracer particle and the electrode must be known. As mentioned earlier, a potential energy balance yielded a 50 nm height for silica target particles. For a tracer particle, the height was taken as the midpoint of the 3 μm thick focal plane. The other parameter is the particle surface conductivity (equation (3.9)). The silica particles have nominal surface potentials of −100 mV under the experimental conditions, but more complicated mechanisms increase this value substantially (Mangelsdorf & White 1990; Rosen, Baygents & Saville 1993). For wont of a more definitive model, the surface conductivity is treated as an adjustable parameter.

Position–time data were computed from the analytical model by means of a first-order explicit forward Euler scheme. For the constant frequency data (figure 12*a*), selection of a surface conductivity $K_s = 1.4 \times 10^{-9}$ S yielded positions in excellent agreement with the experimental observations at all three applied potentials. The agreement between the theory and the experiment for different frequencies (figure 12*b*) was less satisfactory. Use of a K_s value of 1.4×10^{-9} S yields curves that have the correct 'shape', but disagree quantitatively with the data; indeed, no single value of

K_s was able to fit the data. The theory underestimates the velocities at 1000 and 1500 Hz, and overestimates the velocity at 500 Hz.

7. Summary

Analytical expressions were derived for the electric field and corresponding EHD velocity engendered by the presence of a single polarizable particle near an electrode. Numerical calculations for thin double layers and oscillatory fields indicated that a constant field strength electrode boundary condition is a good approximation. The resulting flow structure is toroidal with a far-field radial velocity that decays as r^{-4}. According to the analysis, the direction of flow depends on the particle dipole coefficient. To test the predictions, the motion of fluorescent tracer particles was tracked around a large particle. With the particle surface conductivity treated as the sole fitting parameter, the experimental trajectories accord with the theoretical analysis.

Although the analysis focused on the flow around an individual particle, the underlying behaviour will be found in many-particle systems with smaller particles (Nadal *et al.* 2002; Ristenpart *et al.* 2004). First, the distortion to the electric field on the electrode caused by the presence of the particle diminishes with the particle size. Thus, the constant-field-strength condition is a better approximation for $2\,\mu m$ particles than for the $50\,\mu m$ particles studied here. Likewise, smaller particles reside further from the electrode since the effect of gravity is negligible and the larger value of κh further improves the accuracy of the constant-field-strength condition.

Two aspects of the EHD frequency dependence are noteworthy. First, the decay of the EHD velocity with frequency is consistent with reports of cluster disaggregation at higher frequencies (Trau *et al.* 1996; Solomentsev, Bohmer & Anderson 1997). Although some authors have hypothesized that a reverse in the direction of flow at a critical frequency is responsible for disaggregation (Sides 2001, 2003), no such reverse in flow was observed here experimentally. An alternative hypothesis focuses on dipolar interactions, which are generally not negligible for similarly sized particles. Most authors have attributed observations of repulsive behaviour to dipolar effects (Gong & Marr 2001; Nadal *et al.* 2002; Ristenpart *et al.* 2003, 2004). The monotonically decaying velocity reported here accords with these reports of particle repulsion at higher frequencies, since the attractive EHD flow decays, but the dipolar interaction remains roughly constant over the frequency range of interest. This model also explains observations of stable aggregates with large interparticle separations that are highly sensitive to frequency, but depend very weakly on field strength (Nadal *et al.* 2002; Kim *et al.* 2002), since both dipolar forces and EHD flow scale as E^2.

The second key aspect of the frequency dependence is that the EHD velocity obtained here scales roughly as ω^{-2}, in contrast to the point-dipole analysis presented by Ristenpart *et al.* (2004) where the EHD velocity scales as ω^{-1}. The difference arises from different assumptions, which can be illustrated with the point-dipole scaling expression

$$u \sim C_o' \left(1 + \frac{\kappa^3 D^2}{\omega^2 H} \right) + C_o'' \frac{\kappa^2 D}{\omega}. \tag{7.1}$$

In this work, the Péclet number is assumed to be identically zero, so convection does not affect the electric potential around the particle, i.e. the electric field is changing slowly so the ion distribution can continuously readjust. This effectively sets C_o'' to zero at low frequencies and the inverse-square-frequency dependence predominates. In the point-dipole analysis of Ristenpart *et al.* (2004), however, the standard electrokinetic

model included the effect of convection on the electric potential. For particles with high surface potentials, flow hinders the rearrangement of the ions (Delacey & White 1981) and this yields a phase lag in the potential. Thus, C_o'' is non-zero and the inverse frequency dependency sets in.

Since the kinetic aggregation experiments support an inverse dependence (Kim *et al.* 2002; Ristenpart *et al.* 2004), while the zero-Péclet number approximation employed did not, it appears that the effect of convection on the potential distribution is not unimportant. Inasmuch as $Pe \sim 0.6$ here, this is understandable. More detailed modelling will be required to incorporate this effect. Nonetheless, the close correspondence between the predicted tracer positions and the experimental results indicates that the zero-Péclet number model accurately captures the structure of the EHD flow.

REFERENCES

ANDERSON, J. L. 1989 Colloid transport by interfacial forces. *Annu. Rev. Fluid Mech.* **21**, 61–99.

BAZANT, M. Z. & SQUIRES, T. M. 2004 Induced-charge electrokinetic phenomena: theory and microfluidic applications. *Phys. Rev. Lett.* **92**, 066101.

BHATT, K. H., GREGIO, S. & VELEV, O. D. 2005 An AC electrokinetic technique for collection and concentration of particles and cells on patterned electrodes. *Langmuir* **21**, 6603–6612.

BIKERMAN, J. 1939 Electrokinetic equations and surface conductance: a survey of the diffuse double layer theory of colloidal solutions. *Trans. Faraday Soc.* **36**, 154–160.

BÖHMER, M. 1996 In situ observation of 2-dimensional clustering during electrophoretic deposition. *Langmuir* **12**, 5747–5750.

BRENNER, H. 1961 The slow motion of a sphere through a viscous fluid towards a plane surface. *Chem. Engng Sci.* **16**, 242–251.

DAI, J. H., ITO, T., SUN, L. & CROOKS, R. M. 2003 Electrokinetic trapping and concentration enrichment of DNA in a microfluidic channel. *J. Am. Chem. Soc.* **125**, 13 026–13 027.

DELACEY, E. H. B. & WHITE, L. R. 1981 Dielectric response and conductivity of dilute suspensions of colloidal particles. *J. Chem. Soc. Faraday Trans. II* **77**, 2007–2039.

DUKHIN, S. S. & SHILOV, V. N. 1980 Kinetic aspects of electrochemistry of disperse systems 2: Induced dipole-moment and the nonequilibrium double-layer of a colloid particle. *Adv. Colloid Interface Sci.* **13**, 153–195.

FAGAN, J. A., SIDES, P. J. & PRIEVE, P. C. 2002 Vertical oscillatory motion of a single colloidal particle adjacent to an electrode in an AC electric field. *Langmuir* **18**, 7810–7820.

GAU, H., HERMINGHAUS, S., LENZ, P. & LIPOWSKY, R. 1999 Liquid morphologies on structured surfaces: from microchannels to microchips. *Science* **283**, 46–49.

GONG, T. & MARR, D. W. M. 2001 Electrically switchable colloidal ordering in confined geometries. *Langmuir* **17**, 2301–2304.

GONG, T. Y., WU, D. T. & MARR, D. W. M. 2002 Two-dimensional electrohydrodynamically induced colloidal phases. *Langmuir* **18**, 10 064–10 067.

GONZALEZ, A., RAMOS, A., GREEN, N. G., CASTELLANOS, A. & MORGAN, H. 2000 Fluid flow induced by nonuniform AC electric fields in electrolytes on microelectrodes. ii. A linear double-layer analysis. *Phys. Rev.* E **61**, 4019–4028.

HAPPEL, J. & BRENNER, H. 1973 *Low Reynolds Number Hydrodynamics*. Noordhoff, Leiden.

HOLLINGSWORTH, A. D. & SAVILLE, D. A. 2003 A broad frequency range dielectric spectrometer for colloidal suspensions: cell design, calibration, and validation. *J. Colloid Interface Sci.* **257**, 65–76.

JACKSON, J. D. 1975 *Classical Electrodynamics*, 2nd edn. John Wiley.

JOANNOPOULOS, J. D. 2001 Self-assembly lights up. *Nature* **414**, 257–258.

KIM, J., GUELCHER, S. A., GAROFF, S. & ANDERSON, J. L. 2002 Two-particle dynamics on an electrode in AC electric fields. *Adv. Colloid Interface Sci.* **96**, 131–142.

MANGELSDORF, C. S. & WHITE, L. R. 1990 Effects of Stern-layer conductance on electrokinetic transport-properties of colloidal particles. *J. Chem. Soc. Faraday Trans.* **86**, 2859–2870.

MANGELSDORF, C. S. & WHITE, L. R. 1992 Electrophoretic mobility of a spherical colloidal particle in an oscillating electric-field. *J. Chem. Soc. Faraday Trans.* **88**, 3567–3581.

MOON, P. & SPENCER, D. 1988 *Field Theory Handbook: Including Coordinate Systems, Differential Equations, and their Solutions*, 2nd edn. Springer.

MORRISON, F. A. & STUKEL, J. J. 1970 Electrophoresis of an insulating sphere normal to a conducting plane. *J. Colloid Interface Sci.* **33**, 88.

NADAL, F., ARGOUL, F., HANUSSE, P., POULIGNY, B. & AJDARI, A. 2002 Electrically induced interactions between colloidal particles in the vicinity of a conducting plane. *Phys. Rev. E* **65**, 061409.

O'BRIEN, R. W. 1986 The high-frequency dielectric-dispersion of a colloid. *J. Colloid Interface Sci.* **113**, 81–93.

O'BRIEN, R. W. & WHITE, L. R. 1978 Electrophoretic mobility of a spherical colloidal particle. *J. Chem. Soc. Faraday Trans. II* **74**, 1607–1626.

O'KONSKI, C. T. 1960 Electric properties of macromolecules. 5. Theory of ionic polarization in polyelectrolytes. *J. Phys. Chem.* **64**, 605–619.

POHL, H. A. 1967 Theoretical aspects of dielectrophoretic deposition and separation of particles. *J. Electrochem. Soc.* **114**, C209.

REED, L. D. & MORRISON, F. A. 1976 Hydrodynamic interactions in electrophoresis. *J. Colloid Interface Sci.* **54**, 117–133.

RISTENPART, W. D. 2005 Electric-field induced assembly of colloidal particles. PhD thesis, Princeton University.

RISTENPART, W. D., AKSAY, I. A. & SAVILLE, D. A. 2003 Electrically guided assembly of planar superlattices in binary colloidal suspensions. *Phys. Rev. Lett.* **90**, 128303.

RISTENPART, W. D., AKSAY, I. A. & SAVILLE, D. A. 2004 Assembly of colloidal aggregates by electrohydrodynamic flow: kinetic experiments and scaling analysis. *Phys. Rev. E* **69**, 021405.

ROSEN, L. A., BAYGENTS, J. C. & SAVILLE, D. A. 1993 The interpretation of dielectric response measurements on colloidal dispersions using the dynamic Stern layer model. *J. Chem. Phys.* **98**, 4183–4194.

RUSSEL, W. B., SAVILLE, D. A. & SCHOWALTER, W. R. 1991 *Colloidal Dispersions*, 1st edn. Cambridge University Press.

SIDES, P. J. 2001 Electrohydrodynamic particle aggregation on an electrode driven by an alternating electric field normal to it. *Langmuir* **17**, 5791–5800.

SIDES, P. J. 2003 Calculation of electrohydrodynamic flow around a single particle on an electrode. *Langmuir* **19**, 2745–2751.

SOLOMENTSEV, Y., BOHMER, M. & ANDERSON, J. L. 1997 Particle clustering and pattern formation during electrophoretic deposition: a hydrodynamic model. *Langmuir* **13**, 6058–6068.

SOLOMENTSEV, Y., GUELCHER, S. A., BEVAN, M. & ANDERSON, J. L. 2000 Aggregation dynamics for two particles during electrophoretic deposition under steady fields. *Langmuir* **16**, 9208–9216.

SQUIRES, T. M. & BAZANT, M. Z. 2004 Induced-charge electro-osmosis. *J. Fluid Mech.* **509**, 217–252.

STIMSON, M. & JEFFERY, G. 1926 The motion of two spheres in a viscous fluid. *Proc. R. Soc. Lond. A* **111**, 110.

STONE, H. A. & KIM, S. 2001 Microfluidics: basic issues, applications, and challenges. *AIChE J.* **47**, 1250–1254.

STONE, H. A., STROOCK, A. D. & AJDARI, A. 2004 Engineering flows in small devices: microfluidics toward a lab-on-a-chip. *Annu. Rev. Fluid Mech.* **36**, 381–411.

TEGENFELDT, J. O., PRINZ, C., CAO, H., HUANG, R. L., AUSTIN, R. H., CHOU, S. Y., COX, E. C. & STURM, J. C. 2004 Micro- and nanofluidics for dna analysis. *Analyt. Bioanalyt. Chem.* **378**, 1678–1692.

TRAU, M., SAVILLE, D. A. & AKSAY, I. A. 1996 Field-induced layering of colloidal crystals. *Science* **272**, 706–709.

TRAU, M., SAVILLE, D. A. & AKSAY, I. A. 1997 Assembly of colloidal crystals at electrode interfaces. *Langmuir* **13**, 6375–6381.

VELEV, O. & KALER, E. 1999 In situ assembly of colloidal particles into miniaturized biosensors. *Langmuir* **15**, 3693–3698.

WHITESIDES, G. M. & GRZYBOWSKI, B. 2002 Self-assembly at all scales. *Science* **295**, 2418–2421.

WHITESIDES, G. M. & STROOCK, A. D. 2001 Flexible methods for microfluidics. *Phys. Today* **54**, 42–48.

YEH, S. R., SEUL, M. & SHRAIMAN, B. I. 1997 Assembly of ordered colloidal aggregates by electric-field-induced fluid flow. *Nature* **386**, 57–59.

ZHANG, K. Q. & LIU, X. Y. 2004 In situ observation of colloidal monolayer nucleation driven by an alternating electric field. *Nature* **429**, 739–743.